Available online at www.sciencedirect.com
SCIENCE @ DIRECT®

International Journal of Heat and Fluid Flow 25 (2004) 1015–1033

International Journal of
HEAT AND FLUID FLOW

www.elsevier.com/locate/ijhff

Numerical study of steady/unsteady flow and heat transfer in porous media using a characteristics-based matrix-free implicit FV method on unstructured grids

Kok Siong Chiem, Yong Zhao *

College of Engineering, School of Mechanical and Production Engineering, Nanyang Technological University, Nanyang Avenue, Singapore 639798, Singapore

Received 27 May 2003; accepted 26 January 2004
Available online 2 April 2004

Abstract

In this study, a high-resolution characteristic-based finite-volume (FV) method on unstructured grids [Int. J. Numer. Method Eng. 50 (2001) 11; Int. J. Heat Fluid Flow 21 (2000) 432] is extended by a matrix-free implicit dual-time stepping scheme for the numerical simulation of steady and unsteady flow and heat transfer with porous media. The method has been used to study the characteristics of a complex problem: flow and heat transfer in a channel with multiple discrete porous blocks, which was originally proposed by Huang and Vafai [J. Thermophys. Heat Transfer 8 (3) (1994) 563]. In addition, flow and heat transfer in a channel partially or fully filled with porous layers and containing solid protruding blocks with constant heat flux on its lower surface are also investigated in details. Hydrodynamic and heat transfer results are reported for both steady and transient flow cases. In particular, the effects of Darcy and Reynolds numbers on heat transfer augmentation and pressure loss are studied. An in-depth discussion of the formation and variation of recirculation is presented and the existence of optimum porous insert is demonstrated. At high Reynolds numbers the flow in the porous channel exhibits a cyclic characteristics although unlike the non-porous channel flow, the cyclic vortex development is only restricted to a small area behind the last solid block, while temperature changes more slowly and does not exhibit cyclic variations over a long period of time. It is shown that for all the cases studied altering some parametric values can have significant and interesting effects on both flow pattern as well as heat transfer characteristics.

Keywords: Unsteady flow and heat transfer; Porous media; Channel flow; Computational fluid dynamics; Characteristics-based scheme; Matrix-free dual time stepping scheme

1. Introduction

Theoretical and numerical investigations of fluid flow and forced convection heat transfer in composite systems containing simultaneously fluid regions and porous regions saturated with the same fluid have increased in recent years. This interest is due to their wide ranges of engineering applications such as direct contact heat exchangers, heat pipes and electronic cooling, etc. It has been demonstrated that the insertion of porous materials can have a positive effect on convection heat transfer. Hadim numerically studied laminar forced convection in fully and partially porous channels with discrete heat sources on their bottom walls (Hadim, 1994). And it was found that smaller Darcy number always resulted in a significant increase in heat transfer. Furthermore a partially porous channel configuration can be as effective as its fully porous counterpart in terms of improving heat transfer if properly designed, while its pressure drop is significantly lower than the latter. Similar studies have also been undertaken by Huang and Vafai (1993a,b, 1994), Vafai and Huang (1994), Fu et al. (1996) and Abu-Hijleh (1997). In particular in the study reported by Huang and Vafai (1994), the model used was a horizontal plate with multiple blocks mounted (shown in Fig. 1). The plates were maintained at constant wall temperature and the fluid entered the channel with a parabolic velocity profile.

---

* Corresponding author. Tel.: +65-67904545; fax: +65-57911859.
E-mail address: myzhao@ntu.edu.sg (Y. Zhao).

0142-727X/$ - see front matter © 2004 Elsevier Inc. All rights reserved.
doi:10.1016/j.ijheatfluidflow.2004.01.005

Nomenclature

a	length of porous insert
c	specific heat
Da	Darcy number, K/H^2
F	inertial coefficient
$\vec{F}_c$	convective flux vector
$\vec{F}_v$	viscous flux vector
H	channel height
h_l	head loss
k	thermal conductivity
K	permeability of the porous medium
L	channel length
Nu	Nusselt number
Pr	Prandtl number, ν_f/α_f
p	pressure
q	heat flux
Re	Reynolds number, $u_{av}H/\nu_f$
R_k	thermal conductivity ratio, k_{eff}/k_f
S_p	source term due to porous insert
t	time
T	temperature
u, v	velocity components in the x- and y-directions
$\vec{U}$	velocity vector
u_{av}	inlet averaging streamwise velocity
W	vector of dependent variables

Greeks

α	thermal diffusivity
β	artificial compressibility
γ	kinetic energy coefficient
ε	porosity of porous medium
λ	binary parameter
λ^k	wave speed
ν	kinetic viscosity
ξ	normal co-ordinate
ρ	density
σ	heat capacity ratio
φ	smoothing coefficient
τ	pseudo-time used in the artificial compressibility method

Superscripts

n	time step counter
*	dimensionless quantity

Subscripts

av	average
b	bulk
eff	Effective
f	fluid
h	homogeneous
i	inlet
o	outlet
w	wall

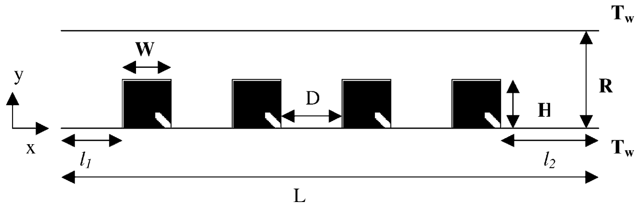

Fig. 1. Schematic of force convection in a parallel plate channel with porous block obstacles.

The Brinkman–Forchheimer-extended Darcy model was used to characterize the flow field inside the porous regions in order to account for both the inertia and viscous effects of the fluid. In order to concentrate on the effect of geometric and thermo-physical variations, the conductivity of the porous media was taken to be equal to that of the fluid. Applying the central differencing for diffusion terms and second-order upwind differencing for the convective terms, the vorticity transport, stream function and energy equations were solved by the control-volume integration of these differential equations over discrete cells. A harmonic mean formulation was used to treat the discontinuous characteristics at the porous/fluid interface. The effects of various flow parameters on forced convection enhancement were analyzed and significant heat transfer augment was achieved. Recently a study of heat transfer enhancement with porous inserts in recirculation region of a flow over a 2D backward-facing step was conducted by Martin et al. (1998), who explored the use of porous inserts for heat transfer enhancement in recirculating flows, especially flow over a backward-facing step using the finite-volume SIMPLER method (Patankar, 1980). It was showed that porous inserts could reduce or eliminate the lower wall recirculation zone (behind the step). However, in some cases the recirculating zone was lengthened if the inserts were short and extremely porous, thus resulting in poorer heat transfer performance with respect to a non-porous duct. More recently Zhang and Zhao (2000, 2001) developed a new high-order characteristics-based finite-volume algorithm on unstructured grids for numerical simulation of incompressible laminar flow and forced convection heat transfer in channels with porous inserts. The method was validated and shown to be accurate, efficient and robust for the study of convection heat transfer in fully and partially porous media.

In this paper, the method developed by Zhang and Zhao (2000, 2001) is extended by a matrix-free implicit dual-time stepping scheme so that the new method can be employed to study not only time-independent problems, but also time-dependent problems efficiently. The method is used to perform a systematic study of thermal convection in the fluid/porous composite system as described by Huang and Vafai (1994) which is found to exhibit very complex and unusual flow and heat transfer phenomena. The main purpose of this study is to further validate the method using such a complex problem and also to gain new insight into the physical aspects of the problem itself (for example, to find out if the flow in this case is time-dependent). Then the method is employed to study another channel flow with multiple protruding blocks and constant heat flux on the lower wall. Both partially and fully porous conditions and their influence on flow separation and circulation are investigated in details. Lastly the Reynolds number is increased and the resulting transient flow and heat transfer in the channel partially filled with porous media is numerically studied.

2. Mathematical model

In this study, it is assumed that the flow is laminar, incompressible and two-dimensional. The porous medium is considered to be homogeneous, isotropic and in local thermo-dynamic equilibrium with saturated fluid. In addition, the thermo-physical properties of the fluid and the solid matrix are assumed to be constant. The governing conservation equations for the problem can then be written separately for the fluid region and porous region. The flow over the fluid region is governed by the incompressible Navier–Stokes equations, while the flow through the porous medium is governed by the generalised momentum equation, which accounts for the effects of the inertia and friction caused by macroscopic shear stress (Zhang and Zhao, 2000, 2001; Hadim, 1994). Here the Brinkman–Forchheimer-extended Darcy model is used to model the flow inside the porous region. These two sets of equations are coupled through matching conditions at the fluid/porous interface. These conditions express continuity of normal and tangential velocities, pressure, normal and shear stresses, temperature, and heat flux.

In this work, the two sets of governing equations are unified into one by introducing a binary parameter (Zhang and Zhao, 2001)

$$\lambda = \begin{cases} 1 \text{ in the porous regions,} & 0 < \varepsilon < 1 \\ 0 \text{ in the fluid regions,} & \varepsilon = 1 \end{cases} \tag{1}$$

λ is set to 1 or 0 in the porous region or no-porous one. When we solve the unified governing equations, the matching conditions at the fluid/porous interface are automatically satisfied, so that the numerical solution procedure is greatly simplified.

The resulting dimensionless governing equations modified by the artificial compressibility method (Zhang and Zhao, 2001) can be expressed as

$$C\frac{\partial W}{\partial \tau} + K\frac{\partial W}{\partial t} + \nabla \cdot \vec{F}_{\mathrm{c}} = \nabla \cdot \vec{F}_{\mathrm{v}} + S_{\mathrm{p}} \tag{2}$$

where

$$W = \begin{bmatrix} p^* \\ [\lambda/\varepsilon - (\lambda - 1)]\vec{U}^* \\ [\lambda(\sigma - 1) + 1]\vec{T}^* \end{bmatrix}$$

$$\vec{F}_{\mathrm{c}} = \begin{bmatrix} [\lambda/\varepsilon - (\lambda - 1)]\beta\vec{U}^* \\ [\lambda/\varepsilon^2 - (\lambda - 1)]\vec{U}^*\vec{U}^* + p^*\delta_{ij} \\ T^*\vec{U}^* \end{bmatrix}$$

$$\vec{F}_{\mathrm{v}} = \begin{bmatrix} 0 \\ [\lambda/\varepsilon - (\lambda - 1)]\frac{1}{Re}\left(\frac{\partial u_i^*}{\partial x_j^*} + \frac{\partial u_j^*}{\partial x_i^*}\right) \\ [\lambda(R_k - 1) + 1]\frac{1}{PrRe}\nabla T^* \end{bmatrix}$$

$$S_{\mathrm{p}} = \begin{bmatrix} 0 \\ \lambda\left(\frac{1}{DaRe} + \frac{F}{\sqrt{Da}}|\vec{U}^*|\right)\vec{U}^* \\ 0 \end{bmatrix}$$

$$\mathbf{K} = \begin{bmatrix} 0 & 0 & 0 \\ 0 & 1 & 0 \\ 0 & 0 & 1 \end{bmatrix}, \quad \mathbf{C} = \begin{bmatrix} \frac{1}{\beta} & 0 & 0 \\ 0 & 1 & 0 \\ 0 & 0 & 1 \end{bmatrix}$$

Here $\vec{F}_{\mathrm{c}}$ and $\vec{F}_{\mathrm{v}}$ are the convective and viscous flux vectors respectively; S_{p} is the source term due to the presence of porous medium; β is a constant called artificial compressibility whose value affects the solution convergence. Note that the field variables in the porous region are volume-averaged quantities as described by Vafai and Tien (1981).

The dimensionless variables used in above equations are defined as follows

$$t^* = \frac{t}{H/u_{\mathrm{av}}} \quad p^* = \frac{p - p_{\mathrm{o}}}{\rho u_{\mathrm{av}}^2} \quad T^* = \frac{T - T_{\mathrm{i}}}{qH/k}$$

$$x^* = x/H \quad y^* = y/H \quad u^* = u/u_{\mathrm{av}} \quad v^* = v/u_{\mathrm{av}}$$

$$\sigma = (\rho C)_{\mathrm{eff}}/(\rho C)_{\mathrm{f}} \quad R_k = k_{\mathrm{eff}}/k_{\mathrm{f}}$$

The boundary conditions are such that no-slip and no-penetration boundary conditions are imposed at the solid walls. At the inlet, the incoming fluid has a uniform temperature, and a fully developed laminar flow profile or a uniform velocity is prescribed. At the downstream end of the computational domain, the non-dimensional pressure there is set to zero. The local Nusselt number is evaluated, namely

$$Nu = \frac{qH}{(T_{\mathrm{w}} - T_{\mathrm{i}})k_{\mathrm{f}}} \tag{3}$$

The local dimensionless pressure drop is calculated as

$$\Delta P^{*} = \frac{\Delta p}{1/2\rho u_{\mathrm{av}}^{2}} \tag{4}$$

The average Nusselt number and pressure drop in the channel are obtained by the integration of the local values over the channel length.

3. Numerical approach

The numerical method, using high-order unstructured-grid finite-volume and characteristics-based (CB) scheme for convection flux calculation, has been presented in (Zhang and Zhao, 2000, 2001). An more detailed description of the high-order interpolation for the convective flux calculation and the CB scheme are given in Appendix A.

The 2D equations in (2) are discretized on an unstructured grid. A cell-vertex scheme is adopted here. For every vertex, as shown in Fig. 2, a control volume is constructed using the median dual of the triangular grid. Spatial discretization is actually performed using the integral form of the conservation equations over the control volume surrounding a node or vertex P

$$\mathbf{C}\frac{\partial}{\partial\tau}\int\int_{S_{\mathrm{cv}}}\mathbf{W}_P\,\mathrm{d}S + \mathbf{K}\frac{\partial}{\partial t}\int\int_{S_{\mathrm{cv}}}\mathbf{W}_P\,\mathrm{d}S + \int\int_{S_{\mathrm{cv}}}\nabla\cdot\vec{\mathbf{F}}_{\mathrm{c}}\,\mathrm{d}S + \int\int_{S_{\mathrm{cv}}}\nabla\cdot\vec{\mathbf{F}}_{\mathrm{v}}\,\mathrm{d}S + \int\int_{S_{\mathrm{cv}}}\mathbf{S}_P\,\mathrm{d}S \tag{5}$$

The convection term is transformed in order to introduce the CB scheme using an edge-based procedure

$$\int\int_{S_{\mathrm{cv}}}\nabla\cdot\vec{F}_{\mathrm{c}}\,\mathrm{d}S = \oint_{L_{\mathrm{cv}}}\vec{F}_{\mathrm{c}}\cdot\mathrm{d}\vec{l} = \sum_{k=1}^{\mathrm{nedge}}[(\vec{F}_{\mathrm{c}})_{ij}^{k}\cdot\Delta\vec{l}_k] \tag{6}$$

where *nedge* is the number of the edges associated with vertex P, $(\vec{F}_{\mathrm{c}})_{ij}^{k}$ is the convection flux through the part of control volume boundary (similar to 1-C_{ij}-2 in Fig. 2) whose length is Δl_k.

The viscous term is calculated by a cell-based method

$$\int\int_{S_{\mathrm{cv}}}\nabla\cdot\vec{F}_{\mathrm{v}}\,\mathrm{d}S = \oint_{L_{\mathrm{cv}}}\vec{F}_{\mathrm{v}}\cdot\mathrm{d}\vec{l} = \frac{1}{2}\sum_{i=1}^{\mathrm{ncell}}(\vec{F}_{\mathrm{v}}\cdot\Delta\vec{l}_{\mathrm{p}})_i \tag{7}$$

where $\Delta\vec{l}_{pi}$ is the edge vector of the cell edge opposite to vertex P of the triangle under consideration. Here the $(\vec{F}_{\mathrm{v}})_i$ is calculated at the center of the triangle cell with a vertex P, which can be obtained by using the Green's Theorem based on the variables at the three vertices of the triangle. The gradient of a flow variable Φ at the center of a cell is evaluated as:

$$\nabla\Phi|_{\mathrm{cell}\,i} = \frac{\int\int_{S_{\mathrm{cell}}}\nabla\Phi\,\mathrm{d}S}{\int\int_{S_{\mathrm{cell}}}\mathrm{d}S} = \frac{\int_{L_{\mathrm{cell}}}\Phi\vec{n}\cdot\mathrm{d}l}{\int\int_{S_{\mathrm{cell}}}\mathrm{d}S} \tag{8}$$

where S_{cell} is the area of cell i and L_{cell} is the boundary edges of cell i. For flow variables at a node, the calculation is based on the area (denoted by S) averaging of those at the centers of the surrounding cells:

$$\nabla\Phi|_{\mathrm{node}\,k} = \frac{\sum_{i=1}^{N}(\nabla\Phi|_{\mathrm{cell}\,i}\cdot S_{\mathrm{cell}\,i})}{\sum_{i=1}^{N}S_{celli}} \tag{9}$$

$S_{\mathrm{cell}\,i}$ is the area of the triangular cell i as shown in Fig. 3 and N is the number of cells associated with node k.

For a certain vertex P, the spatially discretized Navier–Stokes equations without the pseudo-time term form a system of coupled differential equations, which may be written as

$$\begin{aligned} C\frac{\partial W_P}{\partial t} &= -\frac{1}{\Delta S_{\mathrm{cv}}}\left\{\sum_{k=1}^{\mathrm{nedge}}[(\vec{F}_{\mathrm{c}})_{ij}^{k}\cdot\Delta\vec{l}_k] - \frac{1}{2}\sum_{i=1}^{\mathrm{ncell}}(\vec{F}_{\mathrm{c}}\cdot\Delta\vec{l})_i\right\} + S_{\mathrm{p}} \\ &= -\frac{Q(W_P)}{\Delta S_{\mathrm{cv}}} + S_{\mathrm{p}} = -R(W_P) \end{aligned} \tag{10}$$

To improve computational efficiency, implicit schemes can be used in order to use the largest possible time step

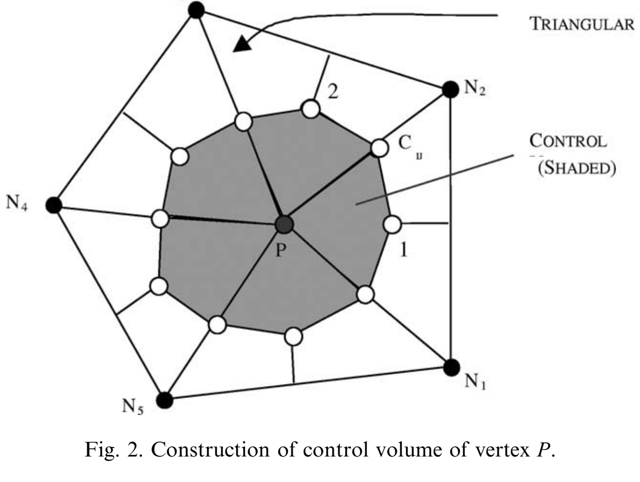

Fig. 2. Construction of control volume of vertex P.

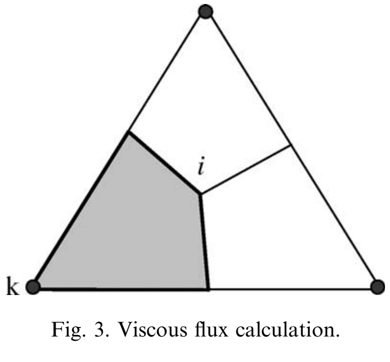

Fig. 3. Viscous flux calculation.

sizes permitted by accuracy consideration. However, most implicit schemes require a large amount of computing effort per time step compared with explicit schemes, making them less attractive for many unsteady flow simulations. Here a matrix-free implicit scheme (Zhao, 2004) is derived, which is found to be efficient in terms of memory required and computing effort per time step. This is due to the fact that no matrix manipulation is required by the scheme.

An implicit scheme is adopted to approximate equation (10) and the semi-discrete form is given as

$$C\frac{\partial}{\partial t}(\Delta S_{\mathrm{cv}} W_P^{n+1}) = -R(W_P^{n+1}) \qquad (11)$$

The superscript $(n+1)$ denotes the time level at $(n+1)\Delta t$ and all the variables are evaluated at this time level. In this work, $\frac{\partial}{\partial t}$ is discretized using a second-order accurate backward differencing formula and Eq. (11) can be rewritten as follows.

$$C\frac{1.5\Delta S_{\mathrm{cv}} W_P^{n+1} - 2.0\Delta S_{\mathrm{cv}} W_P^{n} + 0.5\Delta S_{\mathrm{cv}} W_P^{n-1}}{\Delta t} + R(W_P^{n+1}) = \widetilde{R}(W_P^{n+1}) = 0 \qquad (12)$$

where $\widetilde{R}(W_P^{n+1})$ is the new modified residual which contains both the time derivative and flux vectors.

The advantage of the above implicit scheme is that the physical time step size is not restricted by numerical stability, but only by numerical accuracy. This is especially useful in unsteady flow simulation where the maximum time step size is much smaller than the size permitted by accuracy consideration. The derivative with respect to the pseudo-time τ, is added to the above equation to reformulate the unsteady Navier–Stokes equation as,

$$K\Delta S_{\mathrm{cv}}\frac{W_P^{n+1,m+1} - W_P^{n+1,m}}{\Delta\tau} = \widetilde{R}(W_P^{n+1,m}) \qquad (13)$$

whose solution is sought by marching to a pseudo-steady-state in τ. The superscript $(m+1)$ and (m) denotes time levels in pseudo-time. Once the artificial steady-state is reached, the derivative of W_P with respect to τ becomes zero, and the solution will satisfy $\widetilde{R}(W_P^{n+1}) = 0$. This is actually the solution to Eq. (10). Hence the original unsteady Navier–Stokes equations are fully recovered. Therefore instead of solving each time-step in physical time domain (t), the problem is transferred into a sequence of steady-state computation in the artificial time domain (τ). A matrix-free implicit scheme is derived to solve the discretized NS equations. For details of the scheme, please refer to Appendix A; the efficiency of the scheme has been demonstrated in (Zhao, 2004) for a general flow problem and will not be further discussed here.

4. Results and discussion

4.1. Flow and heat transfer in a channel with porous blocks

The Navier–Stokes equations have been solved numerically for the same case as numerically studied by Huang and Vafai (1994). The motivation here is to further study this complex problem which has some unusual flow characteristics and merits further study. In addition we also want to find out the robustness of the scheme by applying it to such a difficult problem. One thing we can do with the new scheme is to find out if the flow would exhibit any instability at the Reynolds number specified since the method has been extended to perform time marching calculations, which means that both steady and unsteady flows can be calculated automatically. A detailed comparison of streamlines, velocity distribution, isotherms and the quantitative details of Nusselt number distribution across the channel is carried out. The mesh used in Huang and Vafai (1994) was a structured grid with 218×69 cells, which has 15,330 nodes. The basic parameters of the forced convection in the channel with porous blocks emplaced at the bottom wall are $Re = 750$, $Da = 10^{-5}$, $\Lambda = 0.35$, $Pr = 0.7$, $k_{\mathrm{eff}}/k_{\mathrm{f}} = 1.0$, $A = 4$, $B = 1$ and $H^* = 0.25$ (see Fig. 1). In order to obtain mesh independence, we have generated a series of unstructured grids. The results of a 40,000-node mesh are compared with those using 84,000

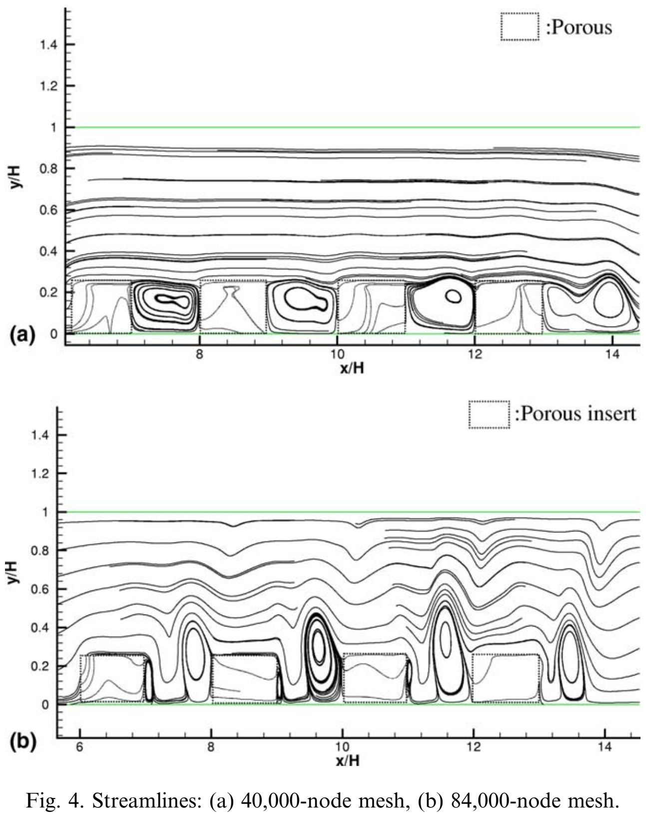

Fig. 4. Streamlines: (a) 40,000-node mesh, (b) 84,000-node mesh.

nodes in Fig. 4. Fig. 4(a) shows the streamlines obtained with the 40,000-node mesh. It has clearly revealed the recirculation behind each porous insert. It is noted that the dimensionless height of each recirculation (y/H) is about the same as the dimensionless height of the porous inserts. By visual inspection, this value of y/H is 0.25. However, when the mesh size is increased to 84,000 nodes, the dimensionless height of the recirculation has increased to 0.58 (see Fig. 4(b)) which is the same magnitude obtained in Huang and Vafai (1994). The authors, Huang and Vafai (1994) had commented on these interesting features of large vortices behind each porous block separated by small recirculation regions rotating in a direction opposite to that of the larger ones. In this study, we observe similar features, but with some differences. For example, the large vortices are confined in the second halves of the space in between two neighboring porous blocks and the counter-rotating ones are in front of the larger ones in the first halves. On the other hand, results in Huang and Vafai (1994) (see Fig. 5) indicate that the large vortices exist in the first halves of the space and they even partially extend into the porous blocks in front and the smaller counter-rotating ones come behind the large ones in the second halves. We believe the latter is less likely to happen than what we obtain because the larger vortices could be easily pushed backwards to the second halves by the high velocity in the non-porous part of the channel above. In addition, with such a low Darcy number the vortices could not easily extend into the porous blocks. The flow is also found to be slightly unstable behind the last porous block.

As it is well known that the number of nodes and computational time are closely related. If there is a need to increase the mesh density for better results, this could be done at the expense of longer computational time. Hence, to minimize computational time, we use point insertion around specific region only. In this case, the selected area is $6 \leqslant x/H \leqslant 13$ and $0 \leqslant y/H \leqslant 0.7$. Then, a brief study is conducted and no more than 1% difference in results is found when the mesh size is increased from 50,000 to 84,000 nodes. As such, a mesh size of 78,000 nodes is chosen. And the final results in terms of streamlines, velocity distribution and isotherm plots are given in Fig. 6. From Fig. 6(a), the height (y/H) of the first three recirculations are 0.5 while the last recirculation is 0.45. In comparison to Fig. 6(a), the height of the four recirculations are the same. As for the velocity distribution and the isotherms, the region inside each porous insert has a flat velocity profile and uniform isotherms in x-direction. This is due to the fact that the porosity of insert used is in the order of 10^{-5}, which results in weak convection and uniform isotherms in x-direction.

A comparison of local Nusselt number distributions of the two studies is shown in Fig. 7(a) (Huang and Vafai, 1994) and Fig. 7(b) (current study). For non-porous channel, both cases show good agreement on numerical values. As for the partially filled porous channel, the first peak in Fig. 7(a) indicates a value of $Nu = 35$, which is slightly lower than the one in Fig. 7(b). The next two peaks in Fig. 7(a) are higher than those in Fig. 7(b), probably due to the different predicted locations of the large vortices. They have an

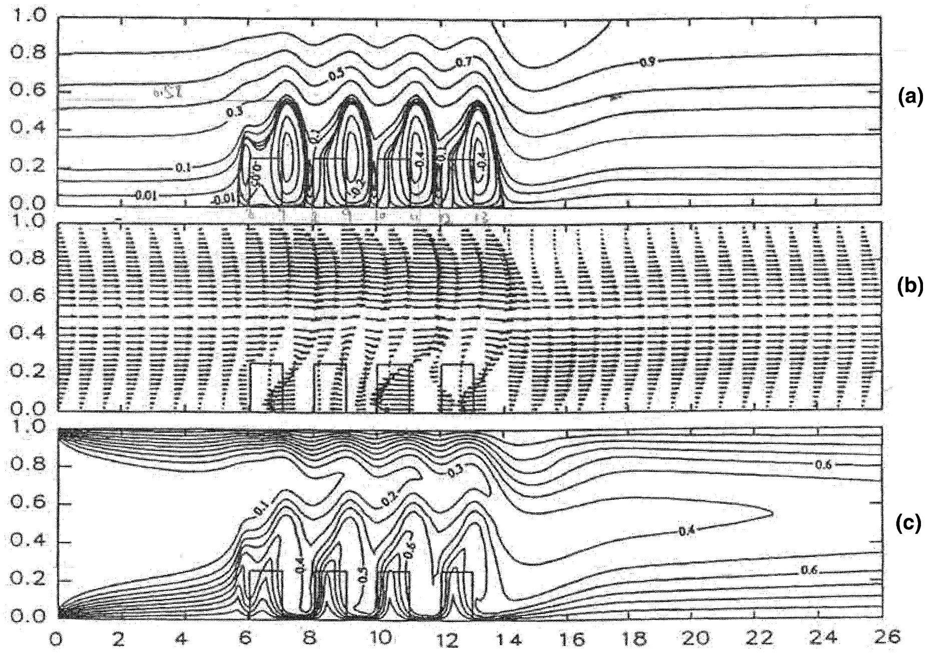

Fig. 5. Results by Huang and Vafai (1994): (a) streamlines, (b) velocity distribution and (c) isotherms.

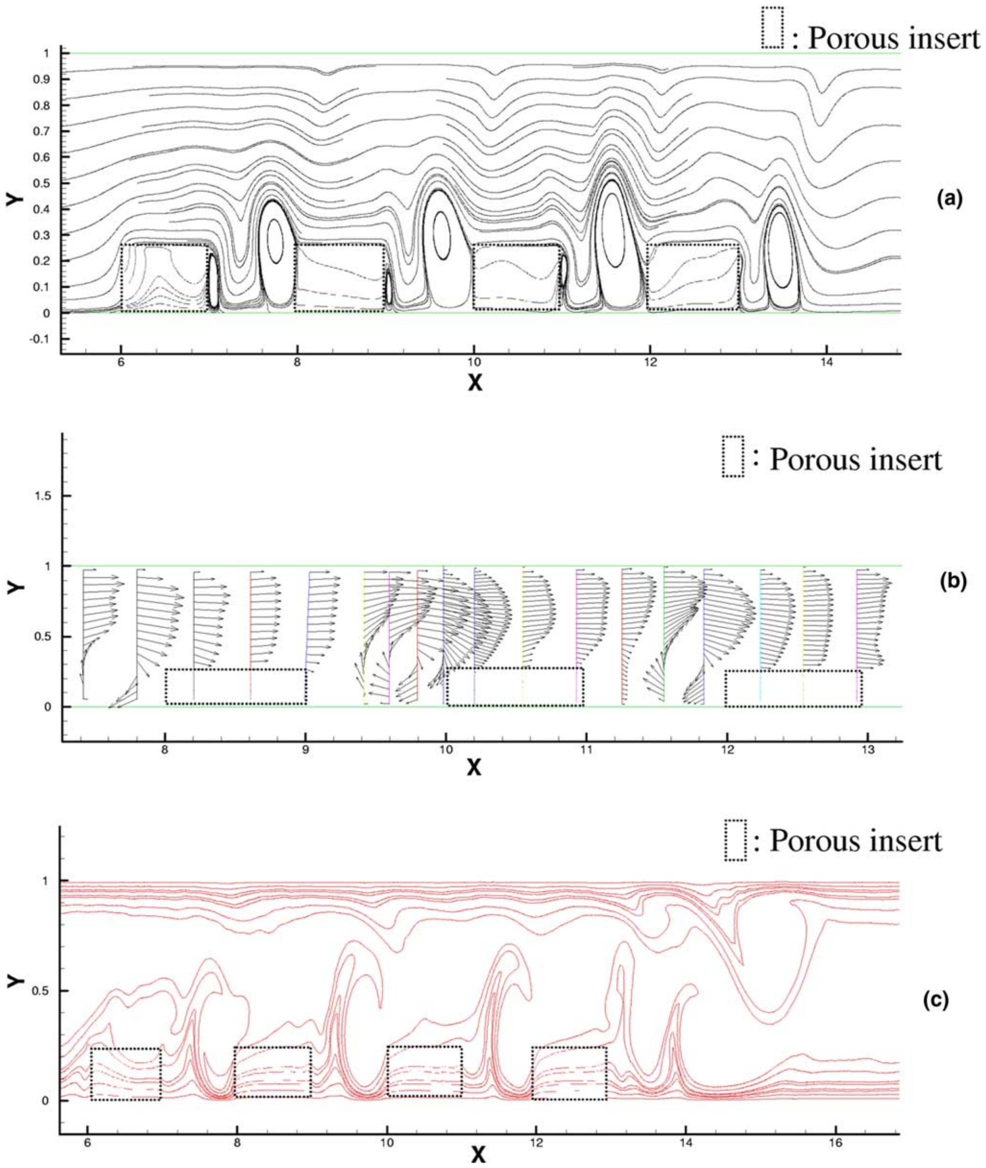

Fig. 6. Final results: (a) streamlines, (b) velocity distribution and (c) isotherms.

average value of 34 while Fig. 7(b) is 30. However, the last peaks are the same, which is just above 30. The overall shapes of the local Nusselt number distribution are similar for both.

4.2. Fully porous channel with protruding solid blocks

In this section, the channel studied is shown in Fig. 8 and all the space is filled with porous media, and the physical parameters used are $Pr = 0.72$ and $\varepsilon = 0.97$. The inflow fluid has a uniform temperature and the lower wall has a constant heat flux. However, the step wall has a fixed temperature which is the same as the in flow temperature. The emphasis of this study is to investigate the influence of some of the parameters, namely Darcy number, Reynolds number, insert dimension and thermal conductivity ratio on the flow field within a simple but well-studied geometry. With a Reynolds number of 900, the effect of different Darcy numbers on the flow and heat transfer in the channel is studied. It is noted that the only variation in the streamline plots shown in Fig. 9 is within the cavities. Fig. 9(b) shows the presence of a full recirculation in the first cavity with $Da = 10^{-2}$. Decreasing the Darcy (Da) number to 10^{-3} and 10^{-4}, i.e. having a lower permeability porous matrix, changes this phenomenon. By comparison Fig. 9(b), (d) and (f) show that the recirculation zone diminishes as Da number decreases. However, the greatest drawback of having small Da number is the high pressure-drop across the channel. The effect of total dimensionless pressure drop with various Da numbers is displayed in Fig. 10. Close

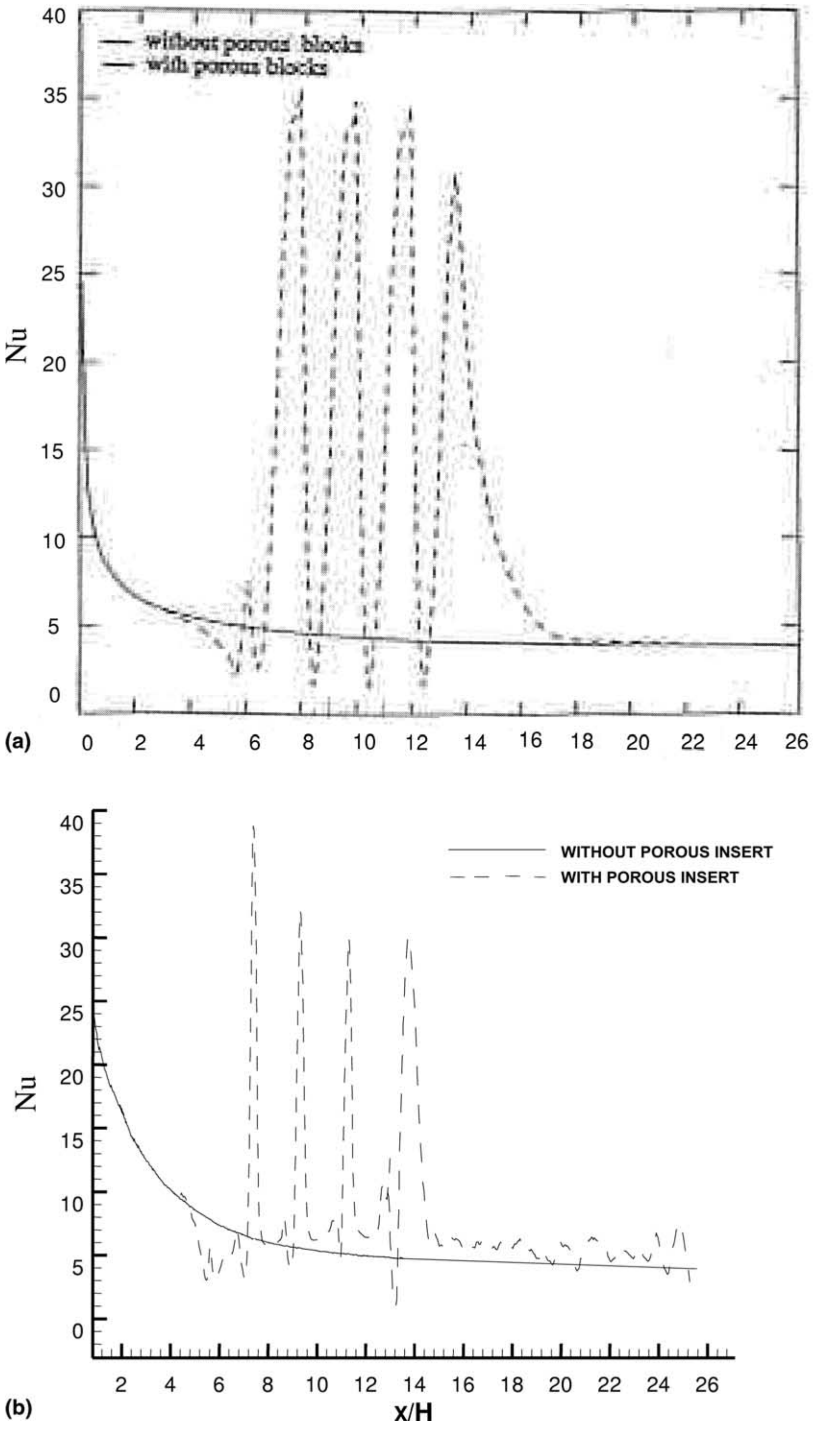

Fig. 7. Local Nusselt number distribution: (a) result from Huang and Vafai (1994); (b) result of present study.

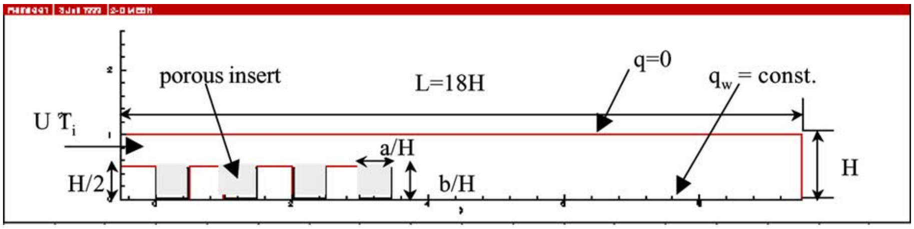

Fig. 8. Dimensions of the channel and porous blocks.

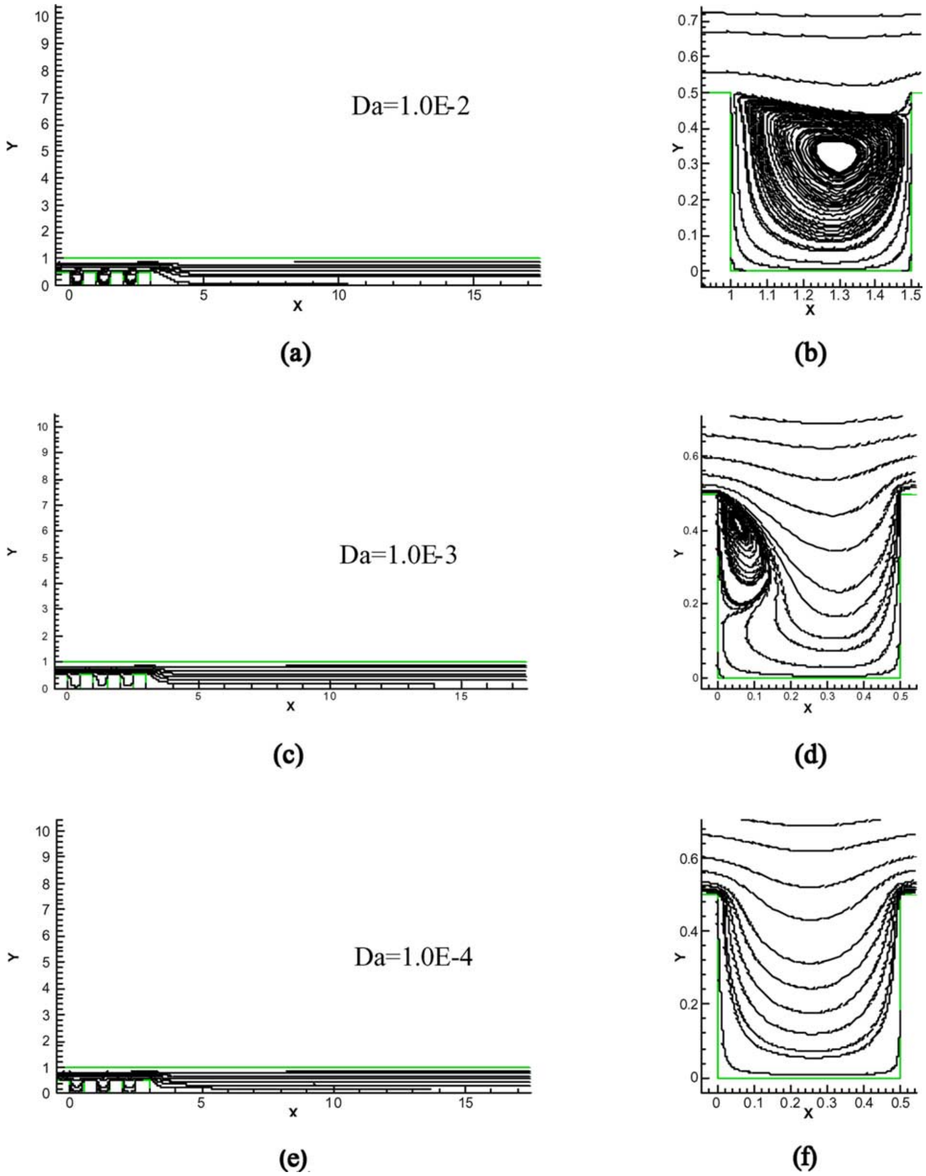

Fig. 9. Streamline plots (a), (c), (e): fully porous channel.

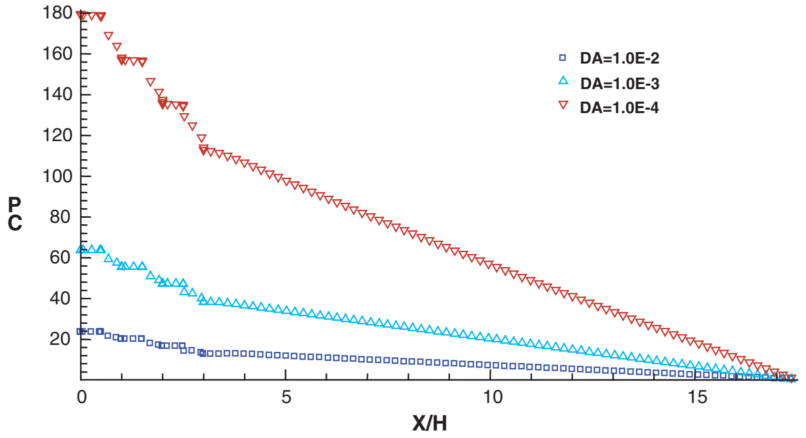

Fig. 10. Effects of total dimensionless pressure drop in the fully porous channel at various Darcy numbers.

examination of Fig. 10 shows that the pressure drop for $Da = 10^{-3}$ is about three times and $Da = 10^{-4}$ is nine times higher than $Da = 10^{-2}$. The conclusion is that pressure drop along the channel increases dramatically as Darcy number decreases.

Fig. 11 illustrates the effects of Darcy number on the bottom wall temperature variation. This distribution always peaks at the leading edge of each cavity where $x/H = 0$, 1.0, 2.0 and 3.0. As for the first cavity, Fig. 11(b) shows that there is a decrease in the wall temperature as *Da* number decreases. This is because for $Da = 10^{-4}$, the recirculation inside the cavity is eliminated (as shown Fig. 9) and those 'trapped' heat is removed by forced convection out of the cavity more easily. It is noted that this phenomenon changes, when the dimensionless horizontal distance (x/H) increases from 0.5 to 1.0 which is the downstream of the cavity, heat coming out of the cavity and reduced convection velocity due to the porous media increase the wall temperature. Thus, the channel with lower permeability porous matrix tends to has higher bottom wall temperature. Therefore, Fig. 11(c) shows that $Da = 10^{-4}$ leads to the highest bottom wall temperature and the distribution drops gradually. The same distribution pattern follows after the step at $x/H = 3.0$ to the end of the channel.

Fig. 12 illustrates the effects of *Da* number on lower wall Nusselt number distribution. For the first cavity, when $Da = 10^{-4}$, Nu_w number is the highest. This implies that h has to be the highest while $(T_w - T_f)$ is the lowest, because $q = h(T_w - T_f) =$ constant. As shown in Fig. 11(b), θ_w is the lowest for $Da = 10^{-4}$ inside the cavity. But for the rest of the channel after the step, it is not the case because wall temperatures are not the lowest but the highest with $Da = 10^{-4}$. Therefore, together with the consideration of pressure drop across the channel, there is a need to find an optimum configuration of the porous matrix in terms of the permeability used and the dimensions of porous inserts. Therefore, the research is extended to study partially filled channel with other permeability and dimensions used.

4.3. Partially porous channel with protruding solid blocks

The same channel as in the last section is used. In the partially porous channel the location of the porous inserts are as follows: $0 \leqslant x/H \leqslant 0.5$, $1.0 \leqslant x/H \leqslant 1.5$, $2.0 \leqslant x/H \leqslant 2.5$ and $3.0 \leqslant x/H \leqslant 3.5$, i.e. they are inserted in the cavities between the solid blocks and behind the last one as well. The effect of variations in the Darcy number is depicted in Fig. 13 for $Re = 900$ and $Da = 10^{-2}$, 10^{-3} and 10^{-4}. Here, an interesting phenomenon happens only when $Da = 10^{-3}$: both the primary and secondary recirculations downstream of the blocks are eliminated due to optimum permeability of the porous media. This is because for smaller *Da* numbers, flow penetration into the porous insert that is located after the step is significantly reduced. When the limit is reached, there is no streamline penetrating the porous block and the flow just passes over the insert like another solid step, after which recirculation starts to form. This is shown in Fig. 13(c), where it is found that the porous block 'pushes' the primary recirculation backward by 0.5H. Similarly the secondary recirculation is being shifted downstream. Similar observations can be made in the cavities, where the degree of recirculation is greatly reduced as the flow just bypasses those cavities and continues its journey downstream.

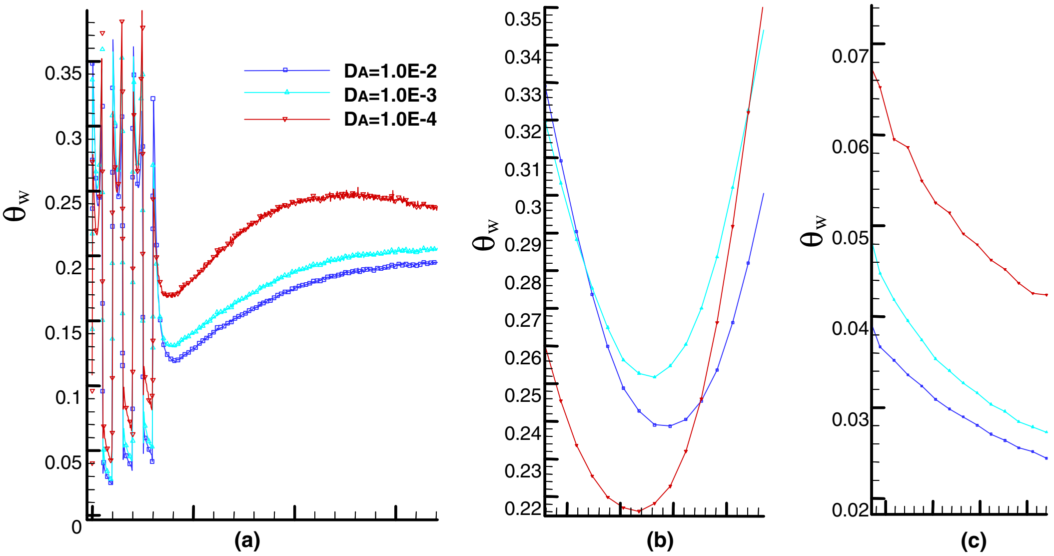

Fig. 11. Effects of Darcy number on the bottom wall temperature variation in the fully porous channel. (a) Whole channel, (b) $0 \leqslant x/H < 0.5$ and (c) $0.5 \leqslant x/H < 1.0$.

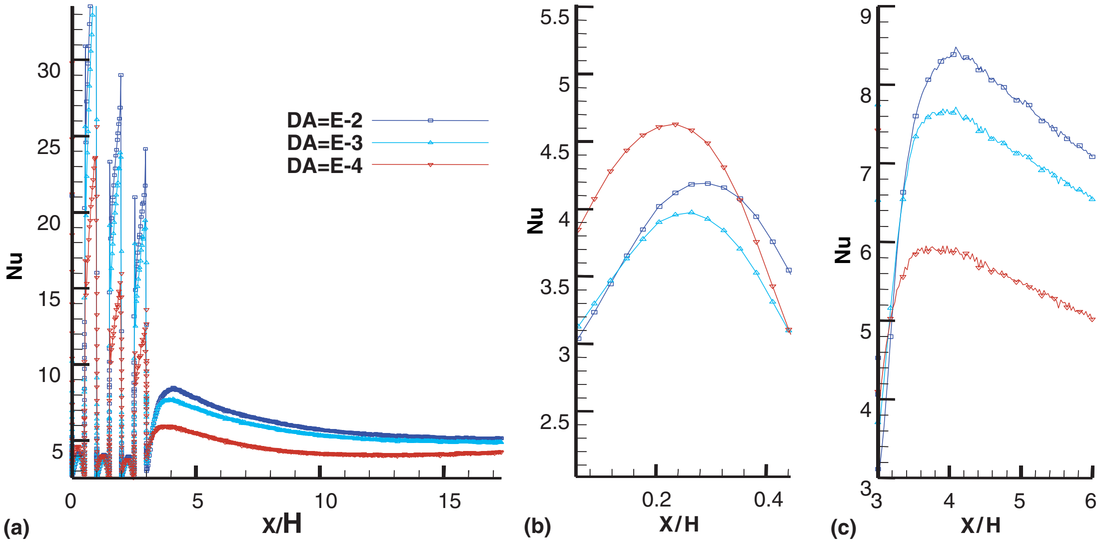

Fig. 12. Effects of *Da* number on lower wall Nusselt number distribution for fully porous channel. (a) Whole channel, (b) first cavity and (c) after the step.

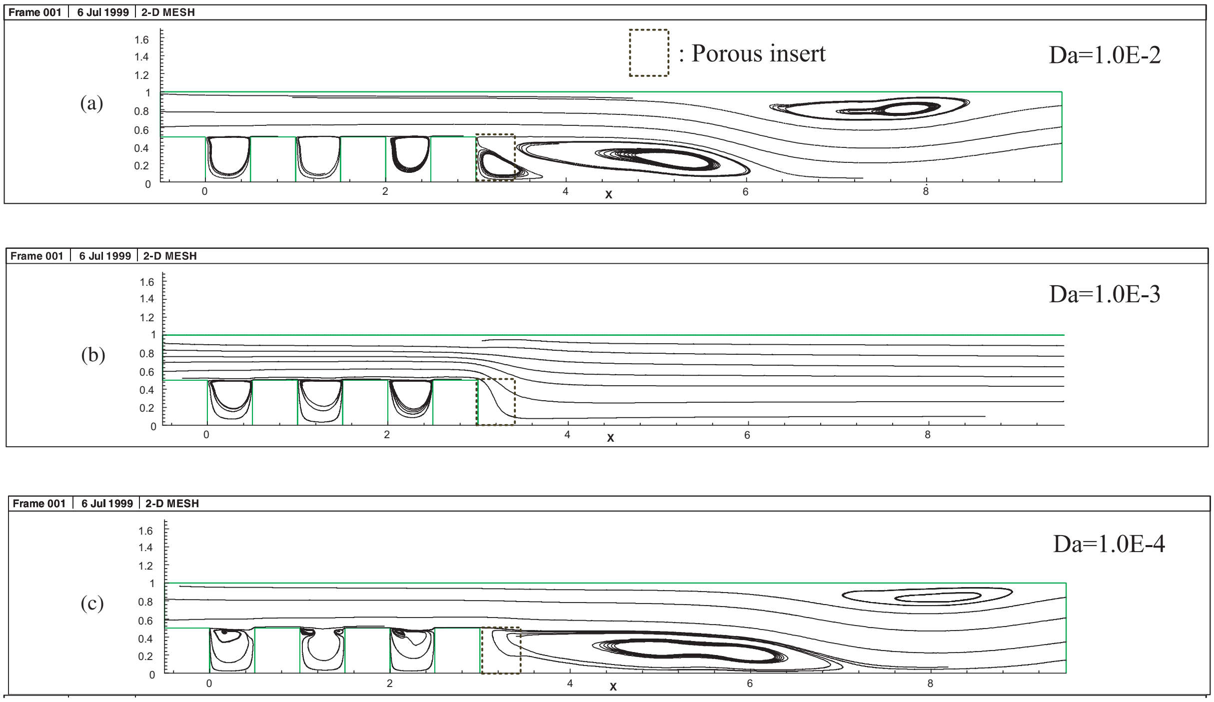

Fig. 13. Streamline plots for $a/H = 0.5$ and $b/H = 0.5$ in the partial porous channel.

The variation of dimensionless lower wall temperature (θ_w) is displayed in Fig. 14 and it is seen that the Darcy number has a significant impact on the temperature distribution. Especially when $Da = 10^{-3}$, θ_w is the lowest after the step. This is due to the elimination of recirculations after the step. Unlike the previous case, θ_w is the highest for $Da = 10^{-4}$ inside the cavity, due to the weakest recirculation inside. Since dimensionless wall temperature (θ_w) is inversely proportional to the lower wall Nusselt number distribution (Nu_w), it is essential to study the Nusselt number distribution in order to understand the effects of convection across the channel. Fig. 15 shows the distribution of the Nu_w number along the lower wall of the channel. Here there is an interesting overall trend in the Nu_w number distribution. There exists an optimum *Da* number (10^{-3}) corresponding to the largest values of the Nu_w number. From Fig. 15(a), at $x/H = 4.0$ onwards, the Nu_w number decreases

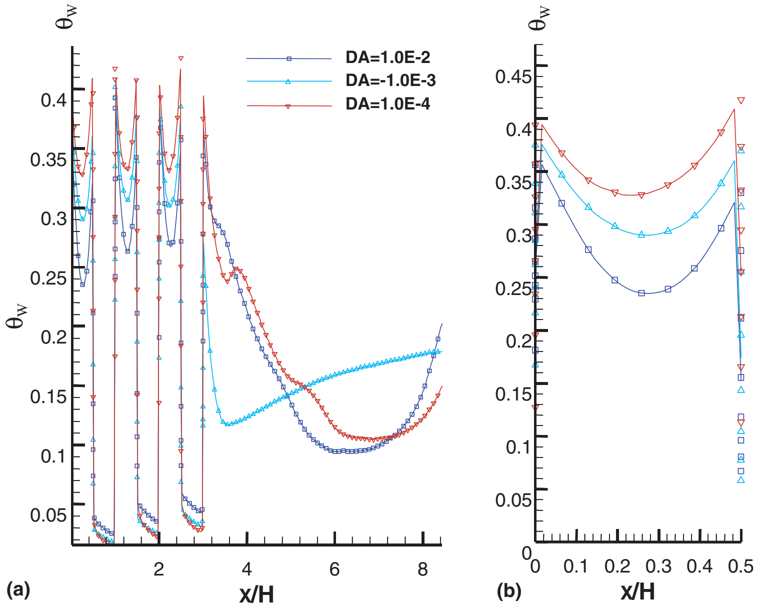

Fig. 14. Effects of the Darcy number on the bottom wall temperature variation in partially porous channel ($a/H = b/H = 0.5$). (a) Whole channel and (b) first cavity.

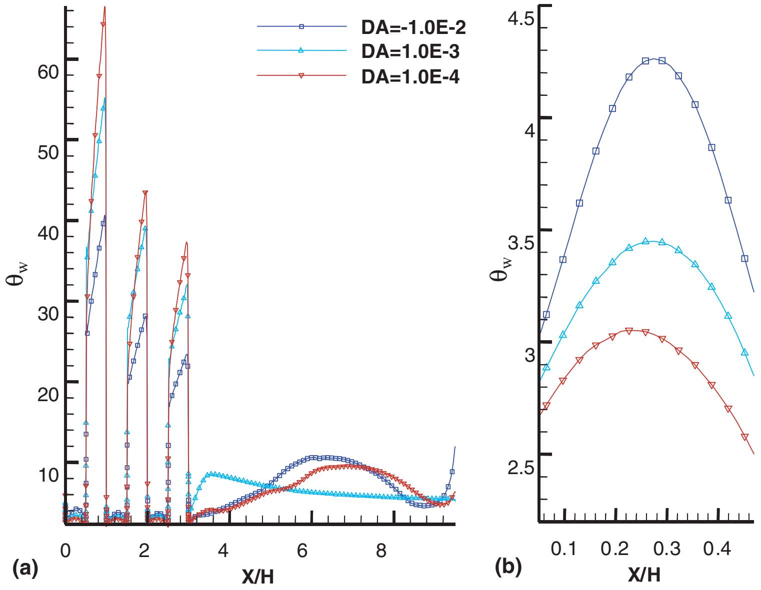

Fig. 15. Effects of the Darcy number on the Nusselt number distribution for partially porous channel ($a/H = b/H = 0.5$). (a) Whole channel and (b) first cavity.

gradually. This is due to the elimination of those two recirculation zones. However, inside the cavities as Da number decreases from 10^{-2} to 10^{-4}, the Nu_{w} number also decreases. With reference to Fig. 15(b), $Da = 10^{-2}$ results in the highest Nu_{w} number in the cavity, which means that in the cavity there is stronger convection heat transfer, therefore more heat is being removed when Da is reduced. From Fig. 13, we can see that as Da increases, especially $Da = 10^{-4}$, there is a weak recirculation in the cavities, and fluid entering and leaving the cavities are minimum. As a result, this reduces the effect of convection and results in a higher dimensionless wall temperature. On the other hand, the region outside the cavities has higher Nu_{w} as there is strong convection over the region.

From the streamline plots and the Nusselt number distribution in the partially porous channel ($a/H = b/H = 0.5$, homogeneous case), $Da = 10^{-3}$ seems to be

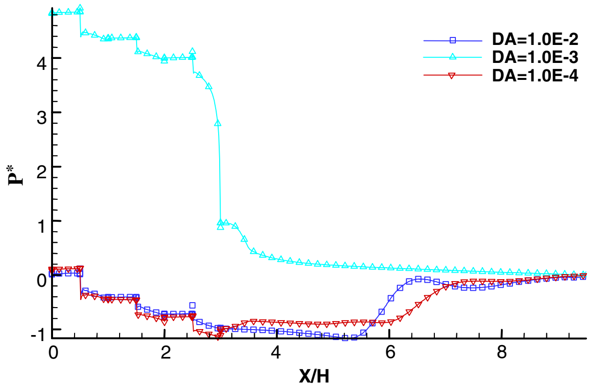

Fig. 16. Effects of total dimensionless pressure drop in partially porous channel at various Darcy numbers ($a/H = b/H = 0.5$).

the optimum value to be used as it successfully eliminates all recirculations and also significantly enhances heat transfer in the channel. The next area of interest is the pressure drop across the channel. Fig. 16 shows the effects of dimensionless pressure drop (P^*), with $Da = 10^{-3}$ resulting in the greatest pressure drop across the channel.

4.4. Unsteady flow in the partially porous channel

For the channel partially filled with porous media, the parameters used are the same as the previous section except that $Re = 1000$. As for the porous inserts, the dimensions of porous used are $a/H = b/H = 0.5$ inside each cavity and $a/H = 0.2$ and $b/H = 1.0$ after the step. This means that the last porous block actually traverse the whole channel and this configuration is found to have greater impact on the flow field. The Darcy number is fixed at 10^{-3}.

4.4.1. Non-porous channel

For comparison purposes, we first calculate the channel flow without any porous medium at all. The flow is found to be unsteady and shows a cyclic variation. Fig. 17 shows the streamlines at the third cavity and behind the step at different time instants. Fig. 17(a) clearly shows the recirculation in the cavity and also the primary separated region behind the step. At this time instant, the recirculation insides each cavity has been fully developed. Interestingly, at the bottom corner, a much smaller recirculation (B) of opposite sign to the primary recirculation (A) is spotted. From this instant onwards, there is a constant interaction between these two recirculations. Then, near the upper wall at some distance downstream, another counter-clockwise rotating recirculation (C) is formed. This recirculation is also called secondary recirculation. C begins to show sign of doubling with ‘C_1’ and ‘C_0’. Further down the channel, another recirculation labeled as ‘D_0’, is induced by C_0 at $x/H = 9.57$.

At PT = 340 (see Fig. 17(b)), the primary recirculation indicates features of doubling with ‘A_0’ and ‘A_1’. When this happens, it is noted that ‘B’ becomes smaller in size. Meanwhile, ‘C_1’ has moved downstream with ‘C_0’ disappearing. Similarly, ‘D_0’ has shifted downstream as well. In Fig. 17(c), the streamline plot at this instant shares the same feature as the previous plot. The only difference is a larger horizontal translation of ‘C’ and ‘D’ downstream. At the next instant, in Fig. 17(d), this doubling effect diminishes inside the primary recirculation when ‘A_1’ combines with ‘A_0’. Interestingly, ‘C’ also begins to show sign of doubling with ‘C_2’ forming before ‘C_1’. As ‘D_0’ continues its motion, ‘C_1’ induces another recirculation ‘D_1’ before ‘D_0’. Finally, in Fig. 17(e), ‘D_0’ disappears with ‘D_1’ replacing its position. These four time frames show the development of the unsteady flow insides the non-porous channel and after which the whole cycle repeats itself.

4.4.2. Partially porous channel

Fig. 18 shows the streamlines from PT = 70 onwards when the porous media are inserted. Fig. 18(a) shows the dissipation of the primary recirculation (A). At this time instant, it has moved downstream to $x/H = 4.35$. As the energy dissipation of A continues, this recirculation diminishes. In the next instant, recirculation A shifts forward to $x/H = 3.55$ as shown in Fig. 18(b). With the use of porous inserts, the core flow downstream is less wavy and this exhibits a more steady flow. It is noted that the secondary recirculation (C) near the upper wall is absent, and also within the primary recirculation (A), there is no further separation of the recirculation into another smaller recirculation. Fig. 18(c) clearly shows the growth and expansion of recirculation (A). At this instant, PT = 90, the recirculation inside the cavity has not been fully developed.

From the streamline plots from (d) to (j), there is the same pattern for the development of recirculation (A). To summarize this development, ‘A’ tends to grow and expand till the threshold of energy sustaining the recirculation is reached. Then, the dissipation of energy takes place and the sign of doubling surfaces. After this, the first recirculation tends to grow while the second recirculation tends to diminish in size. The growing recirculation will overtake the position of the second recirculation. When this takes place, doubling effect disappears and there is only one recirculation left. This cycle repeats itself in every time interval of 30.

Fig. 19(a) shows that the variations of temperature along the bottom wall inside the cavity are more gradual. This explains why porous media can be used for generating more uniform temperature on the cavity's bottom wall. The temperature along the cavity's wall increases monotonically with time. In Fig. 19(b), the presence of the primary recirculation causes a steep drop in bottom wall temperature after the step (T_{bw}).

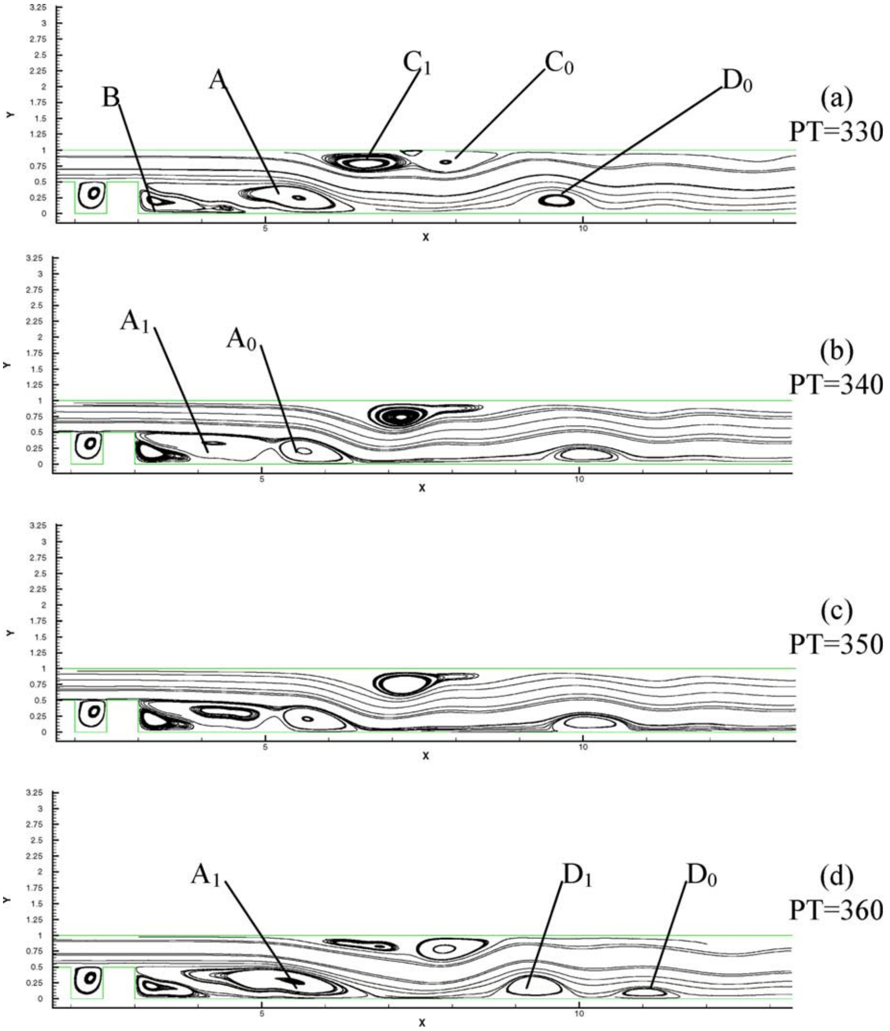

Fig. 17. Flow development inside the non-porous channel.

However, after the recirculation zone, T_{bw} remains a constant. There is no adverse temperature changes along the wall at x/H greater than 5.0. Temperature on the bottom wall keeps increasing from $T = 330$ to 440. Fig. 19(c) indicates a gradual decrease in temperature along the upper wall after the step (T_{uw}). Eventually, T_{uw} reaches a uniform value from x/H equals 10.0 onwards. Different from the previous two plots, the temperature along the upper wall increase suddenly from $T = 330$ to 340, then steadily declines up to $T = 440$.

5. Conclusions

An characteristic-based finite-volume algorithm on unstructured grids is extended by a implicit matrix-free dual-time stepping scheme and applied to analyze steady and unsteady incompressible flow and forced convection heat transfer in channels which are partially and fully filled with porous media. Hydrodynamic and heat transfer results are reported for two cases: (1) flow in a channel with insertion of porous blocks and (2) forced convection in a channel with solid blocks which is fully or partially filled with porous media. In both cases, the characteristics of the flow fields and heat transfer in the channels are greatly changed due to the porous insertion. The effects of Darcy and Reynolds numbers on heat transfer augmentation and pressure loss are investigated. An in-depth discussion of the formation and variation of recirculation is presented and the existence of optimum porous insert is demonstrated. At high Reynolds numbers the flow in the porous channel exhibits a cyclic characteristics although unlike the non-porous channel flow, it is only restricted to a small area behind the last solid block, while temperature changes more slowly and does not exhibit cyclic variations over a long period of time. It is shown that for all the cases studied altering some parametric values can have significant and interesting effects on both flow pattern as well as heat transfer characteristics.

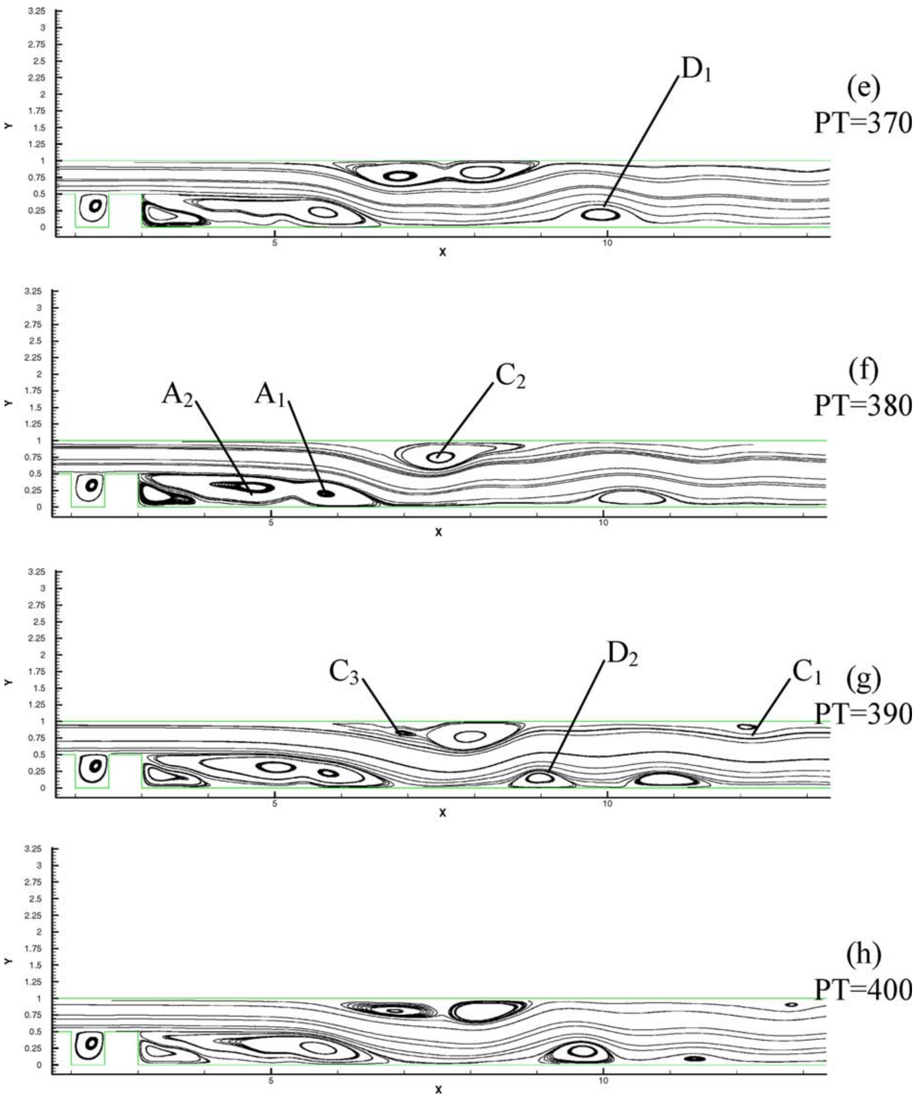

Fig. 17 (*continued*)

Appendix A

The left and right state vectors W_{L} and W_{R} at a section of control volume surface, associated with an edge with two ends i and j, are evaluated using an upwind-biased interpolation scheme (MUSCL)

$$W_{\mathrm{L}} = W_i + \frac{1}{2}[(1-\kappa)\overrightarrow{ij}\cdot\nabla W_i + \kappa\Delta_i^+]$$

$$W_{\mathrm{R}} = W_j - \frac{1}{2}[(1-\kappa)\overrightarrow{ij}\cdot\nabla W_j + \kappa\Delta_j^+]$$

where κ is set to 1/3 which corresponds to nominally third-order accuracy. And

$$\Delta_i^+ = \Delta_j^- = W_j - W_i$$

$$\begin{aligned}\Delta_i^- &= W_i - W_{i-1} = 2\overrightarrow{ij}\cdot\nabla W_i - (W_j - W_i)\\ &= 2\overrightarrow{ij}\cdot\nabla W_i - \Delta_i^+\end{aligned}$$

$$\begin{aligned}\Delta_j^+ &= W_{j+1} - W_j = 2\overrightarrow{ij}\cdot\nabla W_j - (W_j - W_i)\\ &= 2\overrightarrow{ij}\cdot\nabla W_j - \Delta_j^-\end{aligned}$$

Suppose that ξ is a new co-ordinate outward normal to the boundary of a control volume that surrounds a particular vertex. It is assumed that flow in ξ-direction is approximately one-dimensional. In the t-space as shown in Fig. 20, flow variable W at pseudo-time level $n+1$ can be calculated along a characteristics k using a Taylor series expansion and the initial value at time level $n(W^k)$. In the τ–ξ space as shown in Fig. 20, flow variable W at pseudo-time level $n+1$ can be calculated along a characteristics k using a Taylor series expansion and the initial value at pseudo-time level $n(W^k)$

$$W = W^k + W_\xi\xi_\tau\Delta\tau + W_\tau\Delta\tau$$

and

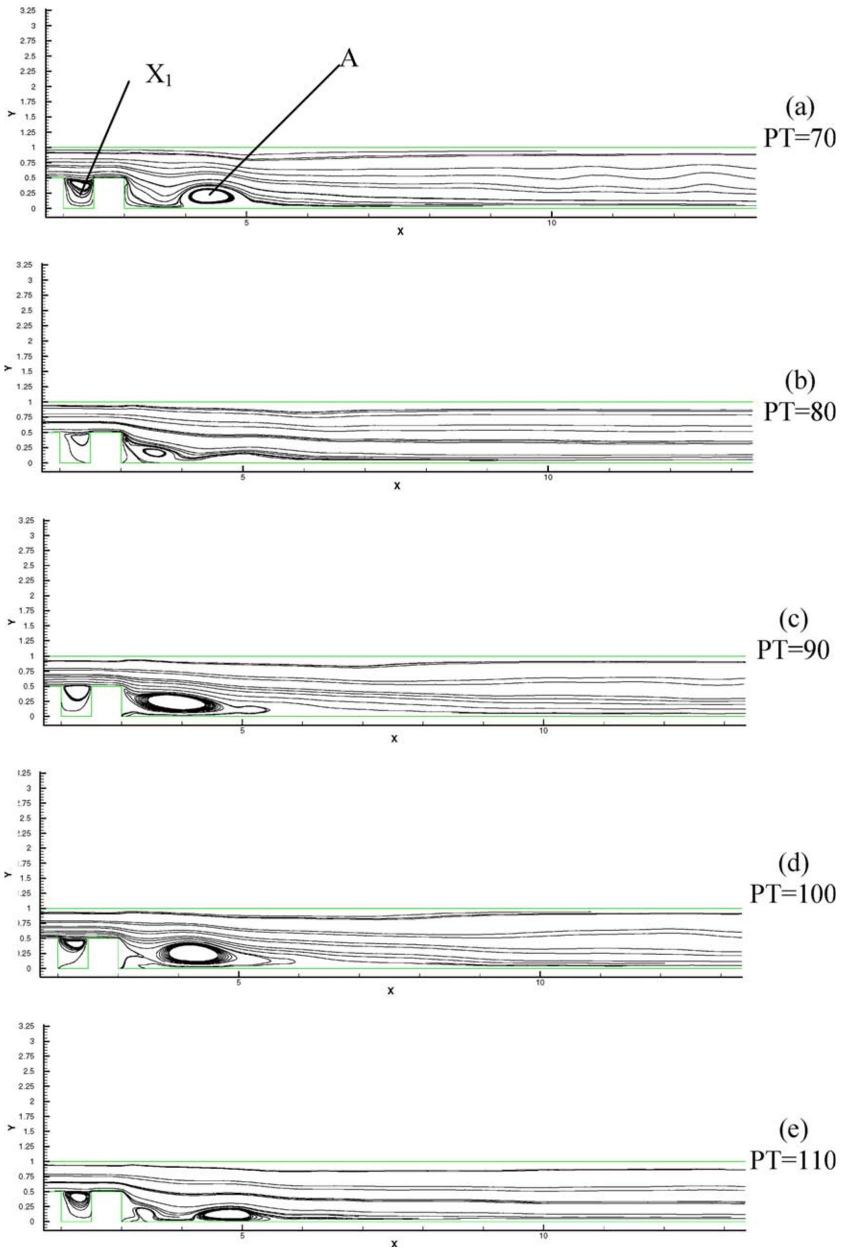

Fig. 18. Flow development inside the partially porous channel.

$$W_\tau = \frac{W - W^k}{\Delta\tau} - W_\xi \xi_\tau$$

A wave speed λ^k is introduced

$$\xi_\tau = \lambda^k \sqrt{\xi_{x_i}\xi_{x_i}}$$

and the normal vector components are

$$n_{x_j} = \xi_{x_j} / \sqrt{\xi_{x_i}\xi_{x_i}}$$

Here a matrix-free implicit scheme is derived to solve the discretized NS equations. All the variables W on the control volume surface (at the center of every edge) at pseudo-time level $n+1$ are determined based on calculations along the characteristics and are then used for convection flux calculations on the control-volume surface (Zhang and Zhao, 2000, 2001). An approximate flux function is introduced here to simplify the implicit time stepping calculation. Following Luo et al. (2001), the total flux (including inviscid and viscous fluxes) across a control-volume surface associated with a certain edge ij can be approximated as

$$F_{ij} \approx \frac{1}{2}\left[\vec{F}_i^c \bullet \vec{n} + \vec{F}_j^c \bullet \vec{n} - |\lambda_{ij}|(W_i - W_j)\right]$$

here λ_{ij} is the spectral radius associated with edge ij:

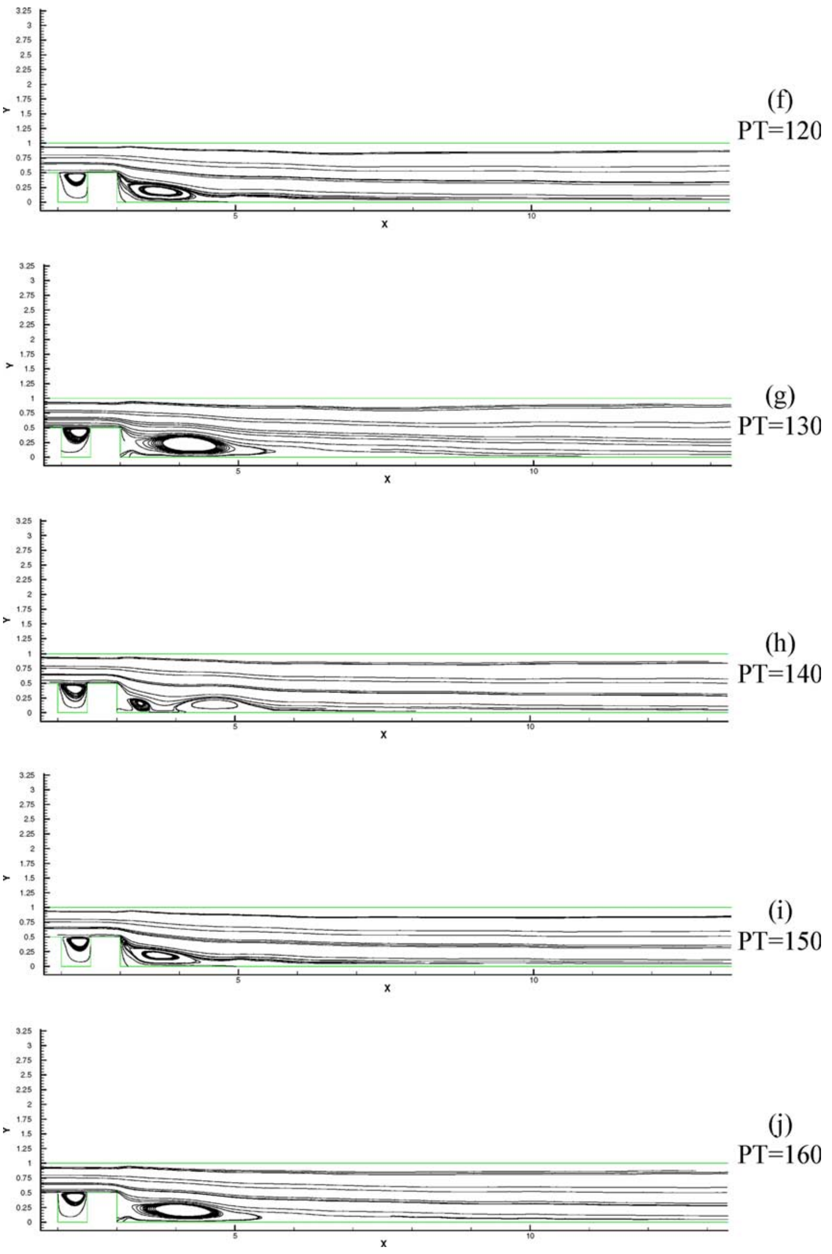

Fig. 18 (*continued*)

$$\lambda_{ij} = \vec{U} \cdot \vec{n}_{ij} + \sqrt{(\vec{U} \cdot \vec{n}_{ij})^2 + \beta^2}$$

A Taylor series expansion is performed for the residual in Eq. (11) with respect to the pseudo-time for node i:

$$\widetilde{R}(W_i^{m+1}) = \widetilde{R}(W_i^m) + \frac{\partial \widetilde{R}_i}{\partial W_i} + \sum_{j=j1}^{jm} \frac{\partial \widetilde{R}_i}{\partial W_j} \Delta W_j$$

And in all the R terms, the Taylor series expansion of the fluxes are

$$\frac{\partial F_{ij}}{\partial W_i} = \frac{1}{2}\left[\frac{\partial F_{ij}^c}{\partial W_i} - |\lambda_{ij}|\right]$$

$$\frac{\partial F_{ij}}{\partial W_j} = \frac{1}{2}\left[\frac{\partial F_{ij}^c}{\partial W_j} + |\lambda_{ij}|\right]$$

And for the physical time-dependent terms, we have

$$W_i^{m+1} = W_i^m + \Delta W_i$$

After combining all the residuals at every node in the flow field into a vector, we have

$$R(W^{m+1,n+1}) = R(W^{m,n+1}) + A\Delta W$$

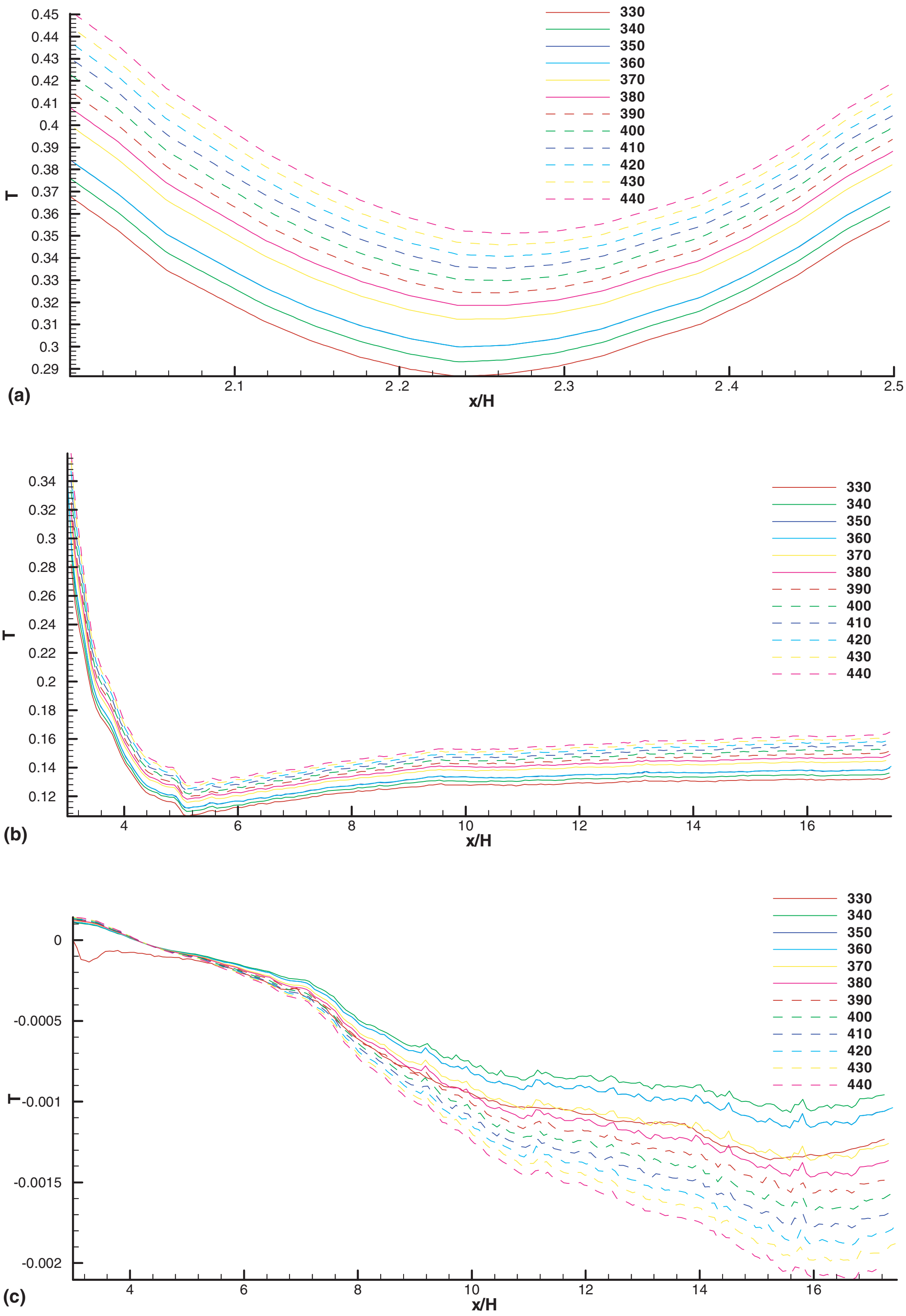

Fig. 19. (a) Bottom wall temperature in cavity. (b) Temperature on bottom wall from $x \geqslant 3.5$. (c) Temperature on upper wall from $x \geqslant 3.5$.

where

$$A = \left\{ \frac{\partial R_i}{\partial W_j} \right\}$$

And the whole-field equivalent of Eq. (13) can then be rewritten as:

$$\Delta S_{\mathrm{cv}}^{n+1}\left(\frac{\Delta t + 1.5\Delta\tau}{\Delta t} - \frac{A\Delta\tau}{\Delta S_{\mathrm{cv}}^{n+1}}\right)\frac{\Delta W}{\Delta\tau} = R^{n+1,m} - \frac{1.5W^{n+1,m}\Delta S_{\mathrm{cv}}^{n+1} - 2.0W^{n}\Delta S_{\mathrm{cv}}^{n} + W^{n-1}\Delta S_{\mathrm{cv}}^{n-1}}{\Delta t} \tag{A.1}$$

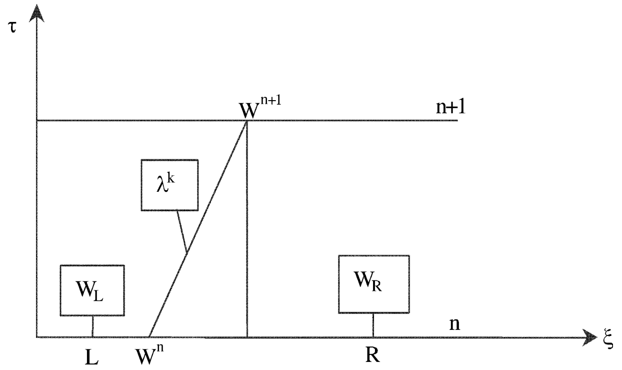

Fig. 20. Characteristics.

i.e.

$$\Delta S_{\text{cv}}^{n+1}\tilde{A}\frac{\Delta W}{\Delta\tau} = \tilde{R}^{n+1,m}$$

Thus

$$\Delta S_{\text{cv}}^{n+1}\frac{\Delta W}{\Delta\tau} = \tilde{\tilde{R}}^{m+1,n}$$

here

$$\tilde{\tilde{R}}^{m+1,n} = \tilde{A}^{-1}\tilde{R}^{n+1,m}$$

$$\tilde{A} = \frac{\Delta t + 1.5\Delta\tau}{\Delta t} - \frac{A\Delta\tau}{\Delta S_{\text{cv}}}$$

$$\tilde{R}^{n+1,m} = \tilde{R}^{n+1,m} - \frac{1.5W^{n+1,m}\Delta S_{\text{cv}}^{n+1} - 2.0W^{n}\Delta S_{\text{cv}}^{n} + W^{n-1}\Delta S_{\text{cv}}^{n-1}}{\Delta t}$$

Further approximation can be introduced in order to achieve matrix-free computation. If we employ point implicit treatment to the above equations, then only the diagonal terms in $\tilde{A}$ is used in the pseudo-time stepping. As a result, Eq. (A.1) for every node can now be written as:

$$\Delta S_{\text{cv}i}^{n+1}\frac{\Delta W_i}{\Delta\tau} = \tilde{\tilde{R}}_i^{m+1,n} \tag{A.2}$$

here

$$\tilde{\tilde{R}}_i^{m+1,n} = \tilde{A}_{ii}^{-1}\tilde{R}_i^{m+1,n}$$

and

$$\tilde{A}_{ii}^{-1} = \left(\frac{\Delta t + 1.5\Delta\tau}{\Delta t} - \frac{A_{ii}\Delta\tau}{\Delta S_{\text{cv}i}}\right)^{-1}$$

Pseudo-time stepping is then performed on Eq. (A.2). For a five-stage scheme, optimum the stage coefficients are

$$\alpha_1 = 1/4, \quad \alpha_2 = 1/6, \quad \alpha_3 = 3/8, \quad \alpha_4 = 1/2, \quad \alpha_5 = 1$$

To speed up convergence rate, an implicit residual-smoothing scheme developed for unstructured grids was employed (Zhang and Zhao, 2000, 2001).

References

Abu-Hijleh, B., 1997. Convection heat transfer from a laminar flow over a 2-D backward facing step with asymmetric and orthotropic porous floor segments. Numer. Heat Transfer, Part A 31, 325–335.

Fu, W.S., Huang, H.C., Liou, W.Y., 1996. Thermal enhancement in laminar channel flow with a porous block. Int. J. Heat Mass Transfer 39 (10), 2165–2175.

Hadim, A., 1994. Forced convection in a porous channel with localized heat sources. J. Heat Transfer 116, 465–472.

Huang, P.C., Vafai, K., 1993a. Flow and heat transfer control over an external surface using a porous block array arrangement. Int. J. Heat Mass Transfer 36, 4019–4032.

Huang, P.C., Vafai, K., 1993b. Passive alteration and control of convective heat transfer utilizing alternate porous cavity-block wafers. Int. J. Heat Fluid flow 15, 275–288.

Huang, P.C., Vafai, K., 1994. Analysis of forced convection enhancement in a channel using porous blocks. J. Thermophys. Heat Transfer 8 (3), 563–573.

Luo, H., Baum, J.D., Lohner, R., 2001. An accurate, fast, matrix-free implicit method for computing unsteady flows on unstructured grids. Comput. Fluids 30, 137–159.

Martin, A.R., Satiel, C., Shyy, W., 1998. Heat transfer enhancement with porous inserts in recirculating flow. J. Heat Transfer 120, 458–467.

Patankar, S.V., 1980. Numerical Heat Transfer and Fluid Flow. Hemisphere, New York.

Vafai, K., Huang, P.C., 1994. Analysis of heat transfer regulation and modification employing intermittently emplaced porous cavities. J. Heat Transfer 116, 604–613.

Vafai, K., Tien, C.L., 1981. Boundary and inertial effects on flow and heat transfer in porous media. Int. J. Heat Mass Transfer 24, 195–203.

Zhang, B., Zhao, Y., 2000. A numerical method for simulation of forced convection in a composite porous/fluid system. Int. J. Heat Fluid flow 21, 432–441.

Zhang, B., Zhao, Y., 2001. Simulation of flow through fluid/porous layers by a characteristic-based method on unstructured grids. Int. J. Numer. Methods Eng. 50 (11).

Zhao, Y., 2004. Computation of complex turbulent flow using matrix-free implicit dual time-stepping scheme and LRN turbulence model on unstructured grids. Comput. Fluids 33 (1), 119–136.